Nuclear Materials and Energy 30 (2022) 101134

Contents lists available at ScienceDirect

Nuclear Materials and Energy

journal homepage: www.elsevier.com/locate/nme

Structural analysis of the optical hinge preliminary design for the ITER wide angle viewing system diagnostic

Santiago Cabrera [a,*], Esther Rincón [a], Mercedes Medrano [a], Frédéric Le Guern [b], Eduardo Rodriguez [c]

[a] CIEMAT, Laboratorio Nacional de Fusión, Avda. Complutense 40, 28040 Madrid, Spain
[b] F4E, Josep Pla 2, Torres Diagonal Litoral B3, 08019 Barcelona, Spain
[c] Department of Construction and Manufacturing Engineering, University of Oviedo, Campus de Viesques, 33203 Gijón, Spain

ARTICLE INFO

Keywords:
ITER diagnostic
WAVS
Optical Hinge
Structural analysis
FEM

ABSTRACT

The ITER Visible/Infrared Wide Angle Viewing System (WAVS) is an optical diagnostic aimed at monitoring the first wall for machine protection purposes. The Optical Hinge (OH) and Optical Relay Unit (ORU) are the first two components in the interspace area and both share a common support structure. The WAVS will be composed by 15 different lines of sight (LoS) distributed around ITER vacuum vessel in Equatorial Ports (EP) 3, 9, 12 and 17. EP12 is currently at its preliminary design and has to be operational for the first plasma. Its development is being carried out by the Consortium constituted by CEA, CIEMAT and Bertin Technologies, within the Framework Partnership Agreement financed by F4E.

The OH mission is to compensate the vertical displacement of the vacuum vessel during operation with respect to the building. Therefore each OH LoS consists of a pair of flat mirrors arranged vertically. The upper one is driven vertically while the other remains fixed. Both mirrors are provided with alignment capabilities to assure their correct installation. The three OH LoS are placed in the OH-ORU common support structure, which is in turn directly attached to the Interspace Support Structure.

In order to assure the optical performance, the OH-ORU common support structure has to withstand thermal and inertial loads during normal operation and SL-1 seism with low deviation (0.3 mm) and tilt (0.5arcmin). In case of Category III and IV (higher seismic or accidental loads) its integrity has to be maintained as it is classified as an ITER Safety Relevant component.

This work comprises the structural analyses performed by CIEMAT of the OH mechanical set to evaluate its optical performance and the ones of the OH-ORU common structure in EP12 to check its integrity in accordance with the RCC-MR Code.

1. Introduction

The ITER Visible/Infrared Wide Angle Viewing System (WAVS) PBS55 G1 is an optical diagnostic aimed at monitoring the first wall for machine protection purposes [1]. It will provide real-time measurements in the visible (656 ± 1 nm) and infrared (4 ± 0.1 μm) spectrum coming from the vacuum vessel [2] to prevent any potential damage in plasma facing components (PFC).

The conceptual design phase was led by ITER Organization [3,4,5,6,7]. That included the Conceptual Design Review passed in 2013 and some latter port and views modifications in 2015 [8,9].

Preliminary design has been developed through a Framework Partnership Agreement between Fusion for Energy (F4E) and a consortium of CEA, CIEMAT (with INTA as third party) and Bertin Technologies company. Preliminary Design Reviews (PDR) of the in-vessel and ex-vessel parts were decoupled and successfully passed in 2020 and 2021.

Current arrange of the diagnostic includes a total of 15 lines of sight (LoS), four in Equatorial Ports (EP) 3, 9 and 17 and three more in EP12 (Fig. 1). Works are firstly focused in EP12 since is the only one that has to be available for the first plasma.

The optical chain of EP12 ex-vessel WAVS is composed of the following subsystems grouped by areas [10]:

* Corresponding author.
E-mail address: santiago.cabrera@ciemat.es (S. Cabrera).

https://doi.org/10.1016/j.nme.2022.101134
Received 30 November 2021; Received in revised form 4 February 2022; Accepted 7 February 2022
Available online 9 February 2022

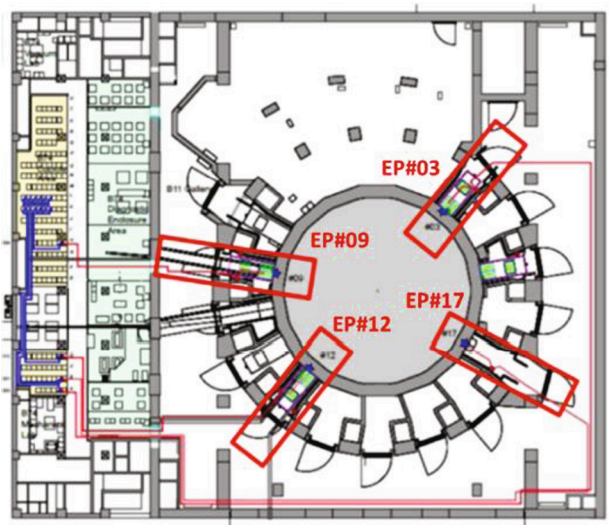

Fig. 1. WAVS general layout.

- In the Interspace (IS)
  - o The Optical Hinge (OH)
  - o The Optical Relay Unit (ORU)
  - o Interspace Afocal Module (IAM)
- In the Bioshield
  - o Cold Dog Leg (CDL)
  - o Objective Unit (OU)
  - o Collimator Unit (CU)
- In the Port Cell (PC)
  - o Port Cell Afocal Module (PCAM)
  - o Shielded Cabinet Components (SCC)

The Optical Hinge (OH) and Optical Relay Unit (ORU) are thus placed in the interspace area and both share a common structure. As member of the Consortium, CIEMAT is in charge of the OH and the common structure while ORU is under CEA responsibility.

This paper summarizes the structural analyses performed for the preliminary design of the OH-ORU common structure and OH mechanical set in EP12 (PBS 55.G1.C0). The aim is to guarantee that the component withstand the loads specified assuring both the structural integrity of the OH-ORU and the optical performance of the OH. This assessment on the structural integrity is made in accordance with the RCC-MR 2007 Code.

2. System description

The WAVS in EP12 is composed by 3 LoS (tangential right, tangential left and divertor). Fig. 2 shows the WAVS subsystems in the interspace.

The whole OH & ORU assembly can be divided in three parts:

- OH and ORU common support structure (OH-ORU): The mechanical structure for the OH and ORU is formed by two vertical parallel plates of irregular shape, 20 mm thick with an inner distance between them of 397 mm. The structure is armed internally by transversal plates where optical components are placed.
- OH: The OH is made up of two flat mirrors per LoS with their corresponding opto-mechanical hardware. To compensate the vertical displacement of the vacuum vessel during normal operation with respect to the building, one mirror (the upper one, called OH1) is driven vertically by means of a piezo actuator and a set of reference switches while the other one is fixed (called OH2). Both mirrors are provided with tilt/tip alignment capabilities. Detailed information about optical design of ex-vessel components can be found in reference [2].

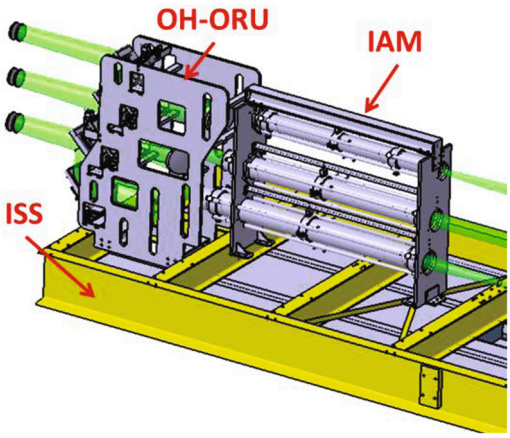

Fig. 2. WAVS subsystems along the interspace.

  - o OH tangential Right view (OH-R)
  - o OH tangential Left view (OH-L)
  - o OH Divertor view (OH-D)
- ORU: The opto-mechanical assembly of a pair off-axis mirrors (ellipsoidal and hyperbolic) for each LoS forming the ORU (3 pairs in total):
  - o ORU tangential Right view (ORU-R)
  - o ORU tangential Left view (ORU-L)
  - o ORU Divertor view (ORU-D)

The support structure of the OH-ORU is directly attached to the Interspace Support Structure (ISS) (Fig. 2). Fig. 3 shows the disposition of the whole assembly with the OH and ORU integrated in the support structure. For further detailed information, all PBS 55.G1.C0 subsystems and components are described in [10,11].

The material used for all the hardware is stainless steel 316L [12] except for the mirrors that are made of Zerodur [13].

3. Loads applied

A document containing System Load Specifications (SLS) for EP12 exvessel WAVS components is approved by ITER for the preliminary design phase [14]. That includes:

- Normal operation loads:
  - o Gravity: the whole OH & ORU assembly weights about 895 kg.

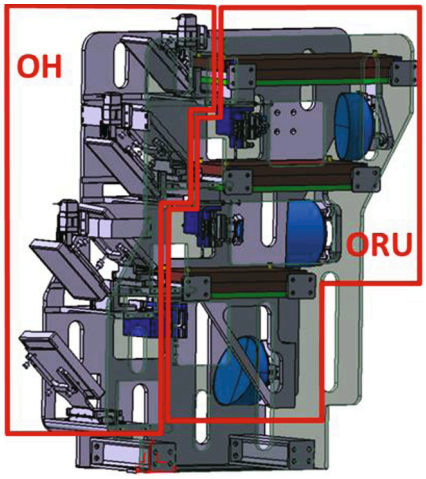

Fig. 3. OH and ORU sub-assemblies integrated in the common support structure.

- o Thermal loads: during normal operation is assumed to be a uniform temperature that ranges from 18 °C to 35 °C.
- Seismic events: components are classified as SC-2 thus SL-1, SMHV and SL-2 levels have to be considered. Equivalent static method was applied with acceleration values summarized in Table 1. In addition, first natural frequency shall be higher than 33 Hz.
- Incident and accident events:
  - o Loss of coolant accident (LOCA): the only LOCA which can affect is the one in the Port Cell as it atmosphere is shared with the interspace. The only effect of the PC LOCA in the system will be a uniform temperature of 145 °C as the overpressure wouldn't cause any effect.
  - o Internal fire: Only the OH-ORU structure, as it is classified as "safety relevant", has to withstand a temperature of 300 °C during 2 h.
- Electromagnetic Loads (EM) due to transient events: according to SLS, EM loads are not expected to be driving loads and were not applied.
- Nuclear heating: is expected to be negligible at the IS area.

Table 2 shows the enveloped load combinations (LC) to be analyzed. The LC corresponding to 18 °C in categories II, III and IV are considered to be enveloped by the 35 °C one. However, the category I 18 °C LC has been considered to evaluate the optical performance in operating conditions.

4. Criteria

4.1. Structural criteria

Structural integrity is assessed for P-type damage in RCC-MR 2007 code, since all the load combinations defined in SLS are permanent or steady varying loads, which are not expected to cause progressive deformation or fatigue.

Elastic analysis method has been applied to all the load combinations, which implies stress linearization to estimate primary membrane intensity (P_m) and bending stresses (P_b), when criteria are not met by the equivalent von Mises stress (VM). Primary stresses ($P_m + P_b$) coming from external mechanical loadings that can lead to rupture, have been differentiated from secondary stresses (Q), coming from internal loadings or imposed displacements, which can disappear as a result of small scale permanent deformations (secondary stresses can be re-distributed because they are surrounded by an elastic environment).

Criteria levels for every category and the corresponding RCC-MR 2007 sections are summarized in Table 3.

In the case of elastic analysis for level A (RB-3251.11) the following conditions must be satisfied:

- The general primary membrane intensity (P_m) should not exceed the maximum allowable stress (S_m) at the mean temperature (θ_m):

$$P_m \leq S_m(\theta_m)$$

- The local primary membrane stress intensity (P_L) should at no time exceed:

$$P_L \leq 1.5 \bullet S_m(\theta_m)$$

Table 1
Seismic equivalent accelerations at PDR phase.

Acceleration component (TGCS)	SL1	SMHV	SL2
ax (m/s^2)	4.4	9.7	13.3
ay(m/s^2)	4.1	9.1	12.4
az(m/s^2)	−14.3	−31.2	−42.8

Table 2
Load combinations to be applied at PDR phase

LC	Weight	Thermal	Event	Category
I.1a	DW	18 °C	–	I
I.1b	DW	35 °C	–	
II.1	DW	35 °C	SL-1	II
III.1	DW	35 °C	SMHV	III
III.2	DW	145 °C	LOCA_PC	
IV.1	DW	35 °C	SL-2	IV
IV.2	DW	300 °C	FIRE	

Table 3
RCC-MR Criteria levels for each load category

	Category I: Operational Loading	Category II: Likely Loading	Category III: Unlikely Loading	Category IV: Extremely Unlikely Loading
Criteria Level	A		C	D
RCC-MR 2007 Section	RB-3251.11		RB-3251.2	RB-3251.3

- The primary membrane plus bending stress intensity should not exceed:

$$P_L + P_b \leq K^* S_m(\theta_m)$$

Where K = 1.5 for shells and plates; K = 1.7 for cylinders; and K = 1.27 for tubes

To comply with level C and D criteria the two first conditions of level A but replacing S_m by:

- Level C: S_m^C defined as the smallest of the two values 1.35 S_m and Minimum yield strength at 0,2% offset $((R\rho_{0.2})_{min})$ calculated for the maximum value of the mean temperature in the thickness
- Level D: S_m^C defined as the smallest of the two values 2.4 S_m and 0.7 Minimum tentile strength $((R_m)_{min},)$ calculated for the maximum value of the mean temperature in the thickness

4.2. Optical tolerances

Optical errors and applicable tolerances due to thermo-mechanical deformations in normal operation, can be classified as follows:

- Decentering: To evaluate the decentering of the mirror respect to the beamline, a coordinate system has been created for each LoS in

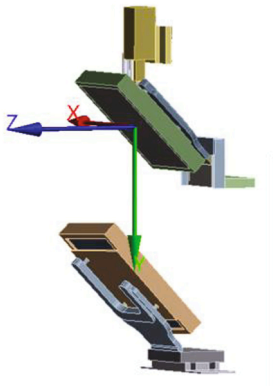

Fig. 4. LoS coordinate systems (decentering).

which the Z axis is aligned with the beamline and X is transversal to it (Fig. 4).

- Mirror tilt: To evaluate the mirror tilt a coordinate system was created for each mirror in which X axis is normal to the mirror surface and Z axis is parallel to its longest edge (Fig. 5). Diagram in Fig. 6 shows how mirror tilt is evaluated. To determine the tilt around Y axis, the difference of displacements in X direction of the upper (X_{Z+}) and lower (X_{Z-}) edges of the mirror is divided by the distance between them (L_Z). The tilt around Z axis is calculated as the difference of displacements in X direction of the edge in positive Y coordinate (X_{Y+}) and the opposite (X_{Y-}) divided by the distance between them (L_Y).
- Changes in the shape of the mirrors. This optical error refers to the deformation of the mirror surface. It is not expected to be relevant in the OH during normal operation, since temperature is uniform throughout the component, and the attachment of each mirror allows it to expand freely, so to keep the original shape

Applicable tolerances to mirror decentering and tilt values during PDR phase are listed in Table 4.

5. FEM model

5.1. Metodology

The analyses have been performed with ANSYS Workbench 2019 R3. Three set of analyses can be distinguished:

1. Modal analysis: To check that the assembly meets the requirement imposed in the SLS that the first natural frequency is higher than 33 Hz.
2. Structural analyses: taking into account that the temperature is assumed to be uniform for thermal and accidental loads and considering that seismic events are evaluated by means of equivalent static method, a static structural analysis has been performed per each load combination listed in Table 2. The objective of these analyses is to evaluate the stresses and displacements for every load combination, to assess the structural integrity of the OH and the OH-ORU common structure at preliminary design.

According to RCC-MR Criteria, in order to isolate the primary stresses to assess P-type damage when thermal loads are applied, the thermal expansion coefficient has been set to zero in the material properties, so that the resulting stresses do not include the secondary ones coming from internal loadings, but only the primary stresses coming from external mechanical loads

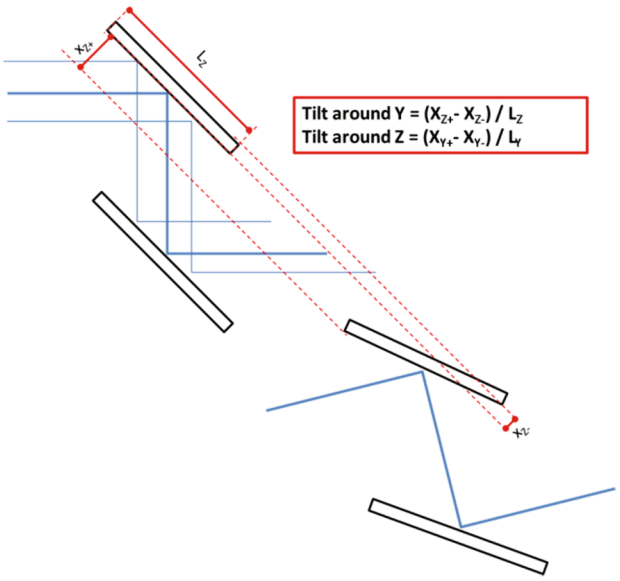

Fig. 6. Mirror tilt definition.

Table 4
Decentering and tilt tolerances in OH mirrors at PDR phase

Decentering (mm)			Tilt (arcmin)	
X	Y	Z	Y	Z
±0.5	±0.3	±0.3	±0.5	±0.5

3. Thermal analyses: the objective of these analyses is to ensure that the optical errors of the OH in normal operation are within the acceptable tolerances [2]. Material thermal expansion was included and only LC I.1a and I.1b of Table 2 were studied.

5.2. Model simplifications

OH-ORU geometry from CAD needs to be simplified for the FEA model, removing those elements and geometrical details that are not relevant for the structural analyses, as shown in Fig. 7. Main simplifications in the overall component are as follows:

- The mechanical support structure is represented using 2D shell elements.
- All pins, bolts and screws have been removed, and the corresponding holes have been filled.

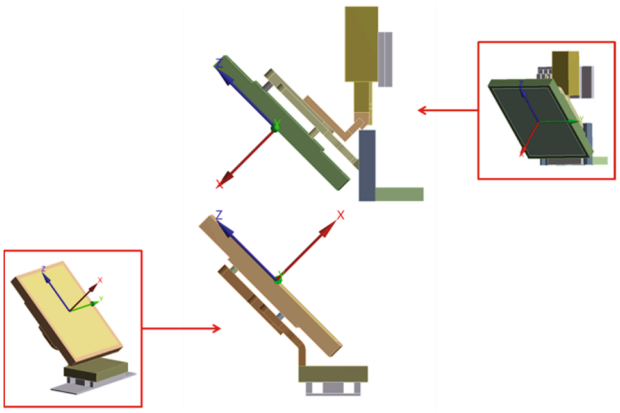

Fig. 5. Mirror coordinate systems (tilt).

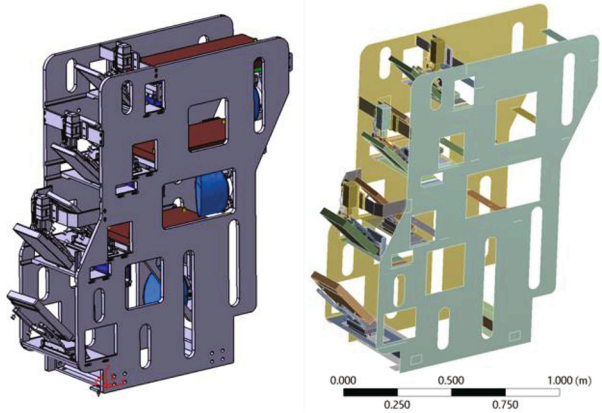

Fig. 7. CAD vs simplified FEA model.

- Bolted connections have been modeled by bonded contacts during the PDR phase. It is expected to analyse the ones with structural relevance for the final design review.
- Linear guides that allow the piezoactuators to move the OH1 mirrors have been replaced by joints allowing only vertical movement (Fig. 8).
- As ORU is not under CIEMAT responsibility, it will not be analyzed within this work. However, it is necessary to take into account its effect to evaluate the common structure behavior. Thus ORU was included as point masses including inertial effects. Since preliminary calculations have shown that ORU divertor LoS first eigenfrequency does not comply with the 33 Hz requirement of SLS, an uncertainty coefficient of 1.2 on the mass of that line was taken into account (but it is out of the scope of this work).

5.3. Mesh

FE mesh for OH-ORU common support structure is made up of 4-node shell elements SHELL181. For the OH mechanical set and mirrors, 3D hexahedral 20-node solid elements SOLID186 are used as preferential. However, 3D tetrahedral 10-node elements SOLID187 are used in some parts, due to their geometrical complexity where the use of hexahedral elements could be problematic or lead to a lesser mesh quality. MASS21 point elements were used to simulate the ORU effect over the common structure. Also MPC184 multipoint constraint elements to attach the ORU point masses and for the joints.

Element size has been reduced to get the highest quality mesh within acceptable computing time limits. The number of nodes and elements are summarized in Table 5.

Mesh verification has been performed in every FEA model run, according to F4E guidelines [15], showing no errors and only 0.68% warnings located in non-relevant areas, so assuring the mesh quality.

An overview of the FE mesh is given in Fig. 9. A detail of OH1 and OH2 mirrors and mountings are shown on Fig. 10a and Fig. 10b respectively.

5.4. Boundary conditions

According to SLS document, since the displacements of the interfaces between the OH-ORU and the ISS were not available at the moment of starting structural integrity assessment for the PDR, these interfaces will be considered as fixed supports in modal and structural analyses Fig. 11.

For thermal loads, SLS considers that the interfaces in the ISS will not impose any restriction to thermal deformations in the component in any direction, since the ISS is fixed isostatically to avoid thermal stresses in the structures, and the thermal expansion coefficients of the components attached to the ISS are similar to those in the ISS. Therefore, boundary conditions for thermal loads consider that only the interface on the lower beam closest to the tokamak centre is fixed (A in Fig. 11), and the rest of lower interfaces have been prevented from moving only in vertical direction (B to D in Fig. 11, allowing their free movement in other directions. Upper ISS interfaces are prevented from moving laterally (B to D in Fig. 11).

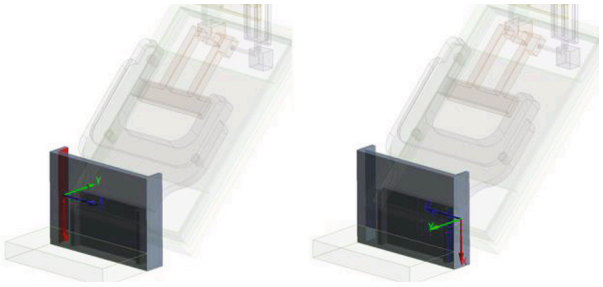

Fig. 8. OH1 mirror (mobile) joints.

Table 5
FE mesh nodes and elements

Number of solid elements	1 360 372
MASS21	3
SHELL181	149 695
MPC184	54
SOLID186	683 893
SOLID187	526 784
Number contact elements	180 844
Number of nodes	4 077 103

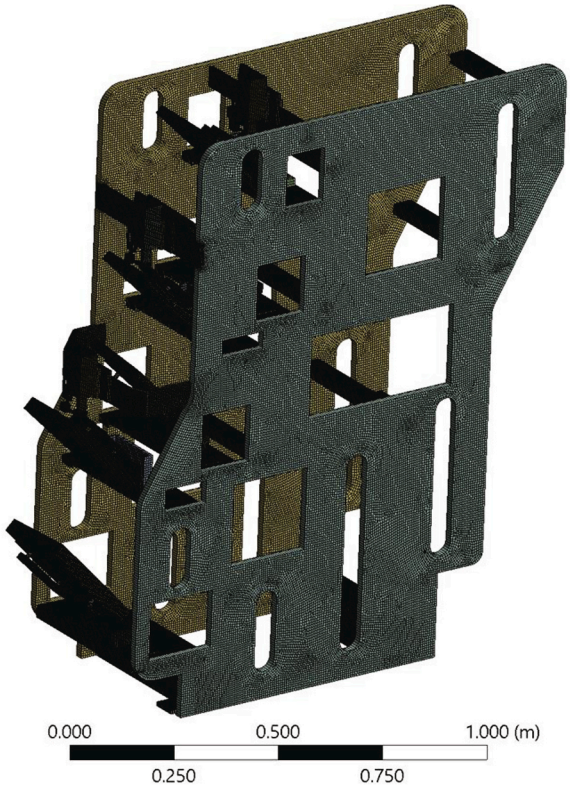

Fig. 9. FE mesh overview.

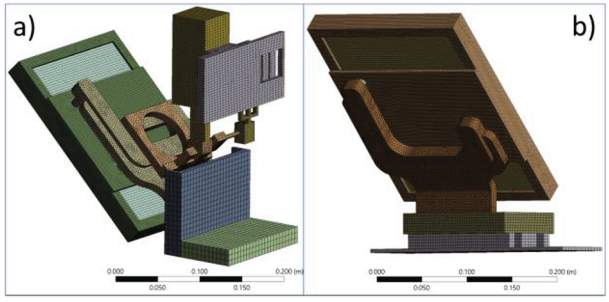

Fig. 10. Detail of OH1(a) and OH2 (b) mounting mesh.

6. Analysis results

6.1. Modal analysis results

Modal analysis has been performed only to confirm that the first natural frequency is higher than 33 Hz. In this case, modal analysis is not relevant to determine seismic loads since SLS imposes the use of the peak value of the FRSs at the building floor, multiplied by 1.5 independently of the natural frequencies.

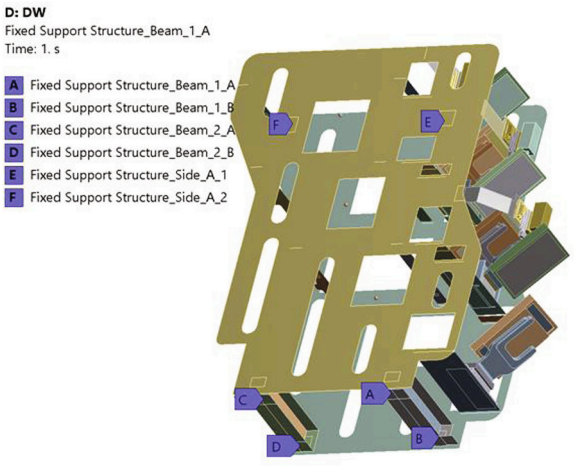

Fig. 11. Fixed supports considered for primary stresses.

A total of 100 natural frequencies have been extracted with a participation mass of 74% to 86% and frequencies between 41.2 Hz and 488.6 Hz. The evolution of the cumulative participation mass is shown in Fig. 12.

Table 6 summarizes the first 10 natural modes, highlighting the dominant ones in which the effective mass involved is higher for each direction.

6.2. OH-ORU common structure stress results

Primary stresses have been analyzed for every LC to assess P-type damage in the OH-ORU common structure. Maximum von Mises primary stresses and the corresponding elastic criteria are summarized in Table 7 for SS316L components.

Maximum primary stresses shown in Table 7 appear on the horizontal structural plate that holds the ORU-R farthest from the tokamak center (Fig. 13 and detail in Fig. 14).

It can be concluded that Primary stresses meet the RCC-MR criteria for the OH-ORU common structure, which means that it will not be subjected to excessive deformation or plastic collapse for any load combination, so assuring the structural integrity of the component for P-type damage.

6.3. OH stress results

Primary stresses have been analyzed for every LC to assess P-type damage in the OH mechanical components. Maximum von Mises primary stresses and the corresponding elastic criteria are summarized in

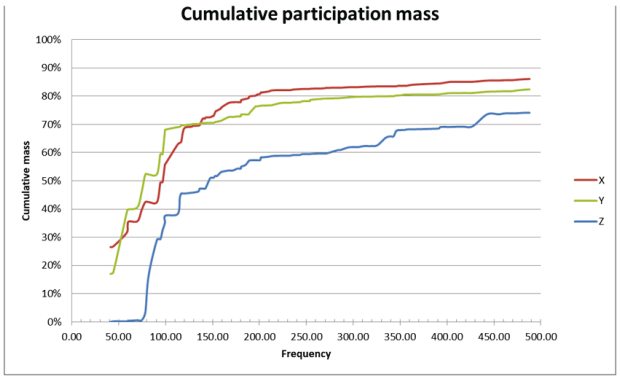

Fig. 12. Cumulative participation mass evolution for modal analyses in each direction.

Table 6
Effective mass ratio of first ten eigenfrequencies in X, Y and Z TGCS directions

Mode	Freq (Hz)	Ratio Effective mass to total mass (%)		
		X direction	Y direction	Z direction
1	41.1	26.52%	17.02%	0.00%
2	44.2	0.24%	0.59%	0.20%
3	58.2	4.72%	20.84%	0.01%
4	59.4	2.52%	1.37%	0.08%
5	60.7	1.61%	0.07%	0.12%
6	70.1	0.13%	0.82%	0.16%
7	74.5	4.00%	5.45%	0.02%
8	78.3	2.75%	6.09%	2.77%
9	81.8	0.01%	0.00%	13.07%
10	90.8	0.01%	0.16%	12.70%

Table 7
Maximum von Mises primary stresses (MPa) in SS316L components

LC	Max VMprimary stress(MPa)	Max allowable stress $S_m(\theta_m)$(MPa)	Elastic criteria for $P_L + P_b 1.5 * S_m(\theta_m)$ (MPa)
I.1b	13.86	127	190
II.1	34.59	127	190
III.1	60.70	171.0	256.5
III.2	13.86	151.5	227.3
IV.1	78.47	304.0	456.0
IV.2	13.86	254.4	381.6

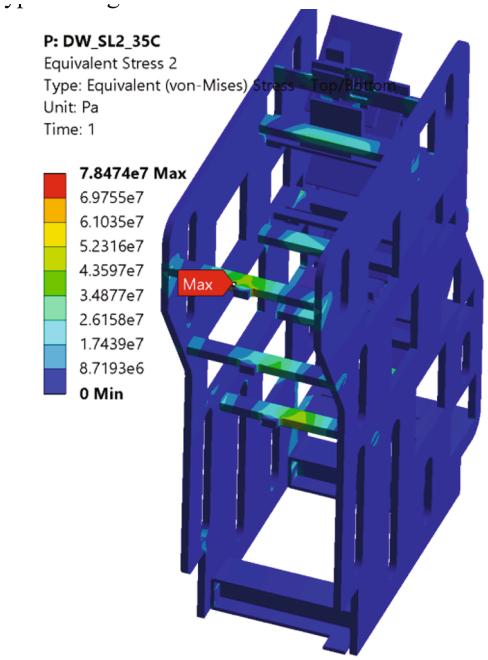

Fig. 13. Structure primary stresses in LCIV.1.

Table 8 for OH1 (mobile mirror) and in Table 9 for OH2 (fixed mirror) components.

In relation to the mirrors, they should be supported in a way that the frame will not induce stress on it. Anyhow, since their final shape and fixation are not included in the CAD model at this preliminary stage, it is not possible to analyze them.

In the case of the OH1 components, the highest stress values appear in the part that connects the mirror frame with the piezoactuator in the divertor LoS (Fig. 15). Stress values meet the RCC-MR limit values.

In the case of the OH2 components, the highest stress values appear in the part that connects the mirror frame to the regulation stages in the divertor LoS (Fig. 16). However, the values are lower than shown for OH1.

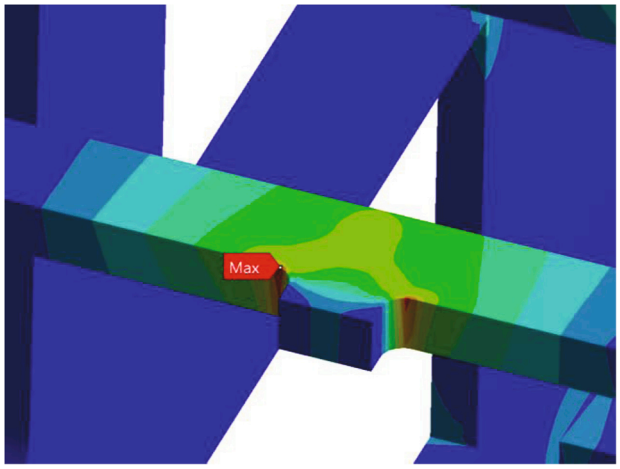

Fig. 14. Detail of primary stresses in LCIV.1.

Table 8
OH1 maximum von Mises primary stresses (MPa)

LC	Max VMprimary stress (MPa)	Max allowable stress S_m	Elastic criteria for $P_L + P_b$
I.1b	11.2	127	190
II.1	26.9	127	190
III.1	45.6	171.0	256.5
III.2	11.1	151.5	227.3
IV.1	58.3	304.0	456.0

Table 9
OH2 maximum von Mises primary stresses (MPa)

LC	Max VMprimary stress (MPa)	Max allowable stress S_m	Elastic criteria for $P_L + P_b$
I.1b	6.0	127	161.30
II.1	21.7	127	161.30
III.1	40.5	171.45	217.70
III.2	6.0	152	193.00
IV.1	53.2	304.8	387.10

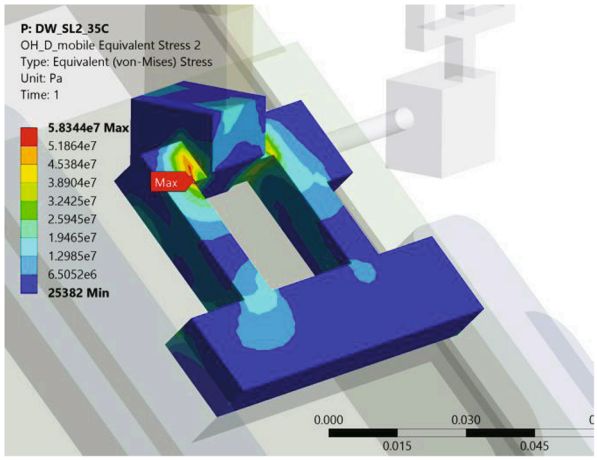

Fig. 15. OH1 maximum primary stresses in LCIV.1.

Therefore, it can be concluded that Primary stresses meet the RCC-MR criteria for every part in the OH, which means that it will not be subjected to excessive deformation or plastic collapse for any load combination, so assuring the structural integrity of the component for P-type damage.

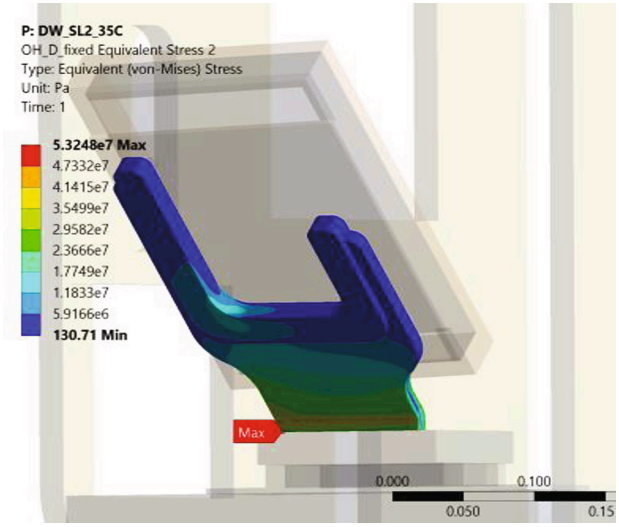

Fig. 16. OH2 maximum primary stresses in LCIV.1.

6.4. *Thermomechanical deformations*

Thermo-mechanical deformations in normal operation have been analyzed, since they are the ones that lead to optical errors. These deformations are due to the variations in the IS room temperature from 18 °C to 35 °C. Fig. 17, Fig. 18 and Fig. 19 represent directional deformations in the X, Y and Z axes respectively due to gravity at 18 °C and at 35 °C. In these results X axis is the direction parallel to EP12 central line (positive getting away from tokamak centre), Z is vertical (positive upwards) and Y is lateral to OH-ORU structure.

Thermal influence in deformations about longitudinal direction (Fig. 17) for the 18 °C LC is very low due to the small temperature difference and deformations are almost the same than with gravity only at 20 °C. However, X deformations are mainly driven by temperature in the 35 °C LC. A clear influence of thermal expansion of the structure can be observed driving the values up to a range of −0.16 to + 0.23 mm.

Deformations in the Y axis (Fig. 18) are also negligible for the 18 °C LC. However, for the 35 °C LC the asymmetry of lateral supports (only placed in the side nearer to the port center) can be clearly observed. The temperature can lead to a lateral displacement of the whole structure up to a tenth of millimeter.

Thermal deformations at 18 °C are insignificant compared to gravity effects. However, weight deformations are thoroughly exceeded by thermal expansion at 35 °C, raising the upper part of the structure 0.35 mm (Fig. 19).

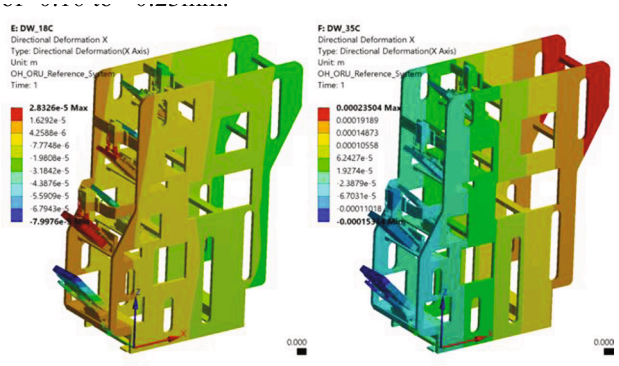

Fig. 17. X deformation (m) in normal operation at 18 °C (left) and 35 °C (right).

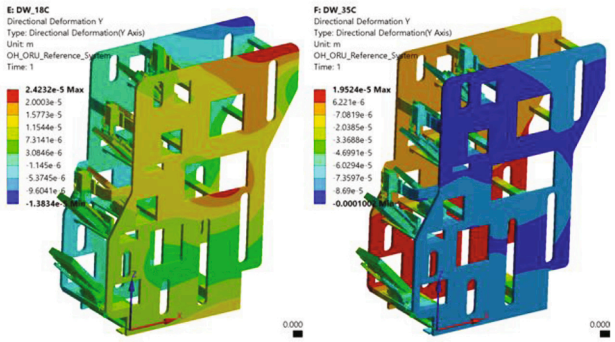

Fig. 18. Y deformation (m) in normal operation at 18 °C (left) and 35 °C (right).

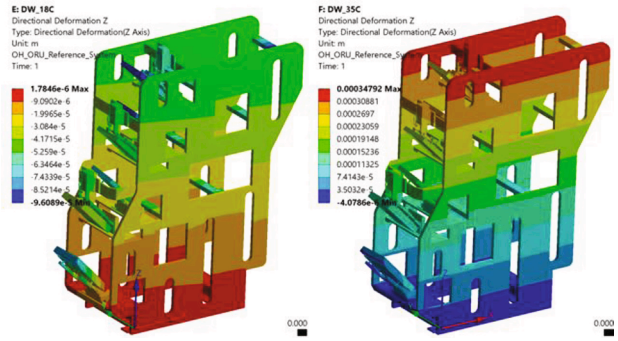

Fig. 19. Z deformation (m) in normal operation at 18 °C (left) and 35 °C (right).

6.5. Optical errors

As the system has to be mounted and calibrated under gravity force, it is assumed that only the thermal deformations will induce errors in normal operation which have to meet the criteria.

Table 10 shows the values corresponding to optical errors for temperatures corresponding to LC in category I. The main deformation of the OH happens in the OH1 mirror of the tangential right LoS as it is placed further from the vertically fixed supports.

Table 11 shows the tilt of the OH mirrors. Highest values appear on tangential right and divertor LoS OH2 mirrors.

Values confirm that optical errors in the OH-L and OH-D are met for tolerance parameters. However, OH-R decentering values are just in the limit and do not comply with tilt optical tolerances. Iterations with the optical design error budget are foreseen and ongoing. They will determine if current decentering and tilt values in OH-R could be assumed by stretching tolerances in other components.

Table 10
Optical decentering

		Decentering X (mm)	Y (mm)	Z (mm)
OH-R				
18 °C	OH1	0.01	0.04	0.00
	OH2	0.01	0.04	0.01
35 °C	OH1	−0.05	−0.30	0.00
	OH2	−0.05	−0.29	−0.06
OH-L				
18 °C	OH1	0.01	0.03	0.00
	OH2	0.01	0.02	−0.01
35 °C	OH1	0.01	0.03	0.00
	OH2	−0.06	−0.19	0.01
OH-D				
18 °C	OH1	0.00	−0.05	−0.05
	OH2	0.01	0.01	−0.01
35 °C	OH1	−0.05	−0.14	0.08
	OH2	−0.04	−0.09	0.05
Tolerance		±0.5	±0.3	±0.3

Table 11
Optical tilt

		Tilt Y (arcmin)	Tilt Z (arcmin)
OH-R			
18 °C	OH1	−0.02	0.00
	OH2	−0.12	−0.01
35 °C	OH1	0.12	0.06
	OH2	0.78	0.09
OH-L			
18 °C	OH1	−0.02	0.01
	OH2	−0.02	0.01
35 °C	OH1	0.15	0.00
	OH2	0.08	0.04
OH-D			
18 °C	OH1	−0.03	−0.05
	OH2	−0.07	−0.01
35 °C	OH1	0.17	0.08
	OH2	0.31	0.05
Tolerance		±0.5	±0.5

7. Conclusions

This paper covers P-type damage assessment for the design of the OH and the OH-ORU common support structure, at the PDR stage. Detailed analysis of the mirror frames, bolts and pins will be analyzed when they are defined in the later stages of the design.

Primary stresses meet the RCC-MR structural criteria defined in Section 4.1. Therefore, the structural integrity for P-type damage is assured.

Natural frequencies calculated in the Modal analysis performed are also acceptable, since their values are higher than the 33 Hz limit defined in SLS.

And finally, thermomechanical deformations and the corresponding optical errors calculated for category I LC (normal operation), in which the WAVS system has to maintain service function, also meet the optical criteria for tangential left and divertor LoS. Tangential right LoS requires future iterations with the optical design error budget in order to re-evaluate the current critical values. Anyway, it has to be taken into account that current limit values are still not definitive and are expected to evolve after the PDR.

In summary, the analyses performed and reported in this paper confirm that the preliminary design of the OH and OH-ORU common support structure is valid to continue with the final design.

Disclaimer

The work leading to this publication has been partially funded by Fusion for Energy under Specific Grant Agreement F4E-FPA 407(DG)-SG04. This publication reflects the views only of the author, and Fusion for Energy cannot be held responsible for any use which may be made of the information contained therein.

CRediT authorship contribution statement

Santiago Cabrera: Conceptualization, Data curation, Formal analysis, Methodology, Visualization, Writing – original draft, Writing – review & editing. **Esther Rincón:** Investigation, Supervision, Writing – review & editing. **Mercedes Medrano:** Project administration, Resources. **Frédéric Le Guern:** Project administration. **Eduardo Rodriguez:** Supervision, Writing – review & editing.

Declaration of Competing Interest

The authors declare that they have no known competing financial interests or personal relationships that could have appeared to influence the work reported in this paper.

References

[1] R. Reichle et al., "On the operational specifications and associated R&D for the VIS/IR diagnostic for ITER," 2009 1st International Conference on Advancements in Nuclear Instrumentation, Measurement Methods and their Applications, 2009, pp. 1-7, 10.1109/ANIMMA.2009.5503692.

[2] Carmen Pastor, et al., Optical design of ex-vessel components for the Wide Angle Viewing System diagnostic for ITER, Fusion Engineering and Design 168 (2021) 112607, https://doi.org/10.1016/j.fusengdes.2021.112607. ISSN 0920-3796.

[3] M. Davi, et al., Progress of the ITER equatorial vis/IR wide angle viewing system optical design, Review of Scientific Instruments 79 (10) (2008) 10F509, https://doi.org/10.1063/1.2958091.

[4] Sophie Salasca, et al., Development of equatorial visible/infrared wide angle viewing system and radial neutron camera for ITER, ISSN 0920-3796, Fusion Engineering and Design 84 (7–11) (2009) 1689–1696, https://doi.org/10.1016/j.fusengdes.2008.12.088.

[5] J. Travere et al., "The ITER VIS/IR wide angle viewing system: Challenges and ongoing R&D," 2011 2nd International Conference on Advancements in Nuclear Instrumentation, Measurement Methods and their Applications, 2011, pp. 1-9, 10.1109/ANIMMA.2011.6172871. https://ieeexplore.ieee.org/abstract/document/6172871.

[6] Sophie Salasca, et al., Recent technical advancements of the ITER Equatorial Visible/InfraRed Diagnostic, ISSN 0920-3796, Fusion Engineering and Design 86 (6–8) (2011) 1217–1221, https://doi.org/10.1016/j.fusengdes.2011.02.015.

[7] R. Reichle, et al., Concept development for the ITER equatorial port visible/infrared wide angle viewing system, Review of Scientific Instruments 83 (2012) 10E520, https://doi.org/10.1063/1.4734487.

[8] Sophie Salasca, et al., The ITER Equatorial Visible/Infra-Red Wide Angle Viewing System: Status of design and R&D, ISSN 0920-3796, Fusion Engineering and Design, Volumes 96–97 (2015) 932–937, https://doi.org/10.1016/j.fusengdes.2015.02.062.

[9] Laurent Letellier, et al., System level design of the ITER equatorial visible/infrared wide angle viewing system, ISSN 0920-3796, Fusion Engineering and Design 123 (2017) 650–653, https://doi.org/10.1016/j.fusengdes.2017.06.005.

[10] M. Medrano, et al., Design overview of ex-vessel components for the Wide Angle Viewing System diagnostic for ITER Equatorial Port 12, ISSN 0920-3796, Fusion Engineering and Design 168 (2021), https://doi.org/10.1016/j.fusengdes.2021.112651.

[11] S. Garitta, et al., Electromagnetic analysis of ITER equatorial Wide Angle Viewing System (WAVS) in-vessel components, ISSN 0920-3796, Fusion Engineering and Design 170 (2021), https://doi.org/10.1016/j.fusengdes.2021.112471.

[12] AFCEN. Design and construction rules for mechanical components of nuclear installations. RCC-MR 2007 Section1, subsection z Appendix A3.

[13] SCHOTT AG Advanced Optics, ZERODUR Zero Expansion Glass Ceramic. Product catalog. https://www.schott.com/en-in/products/zerodur-p1000269/downloads.

[14] F4E-FPA-407 SG04 D10 CD24.2 - PBS 55.G1.C0 System Load Specifications, ex-vessel components (F4E_D_2DAYR7 v4.0).

[15] F4E-QA-114 Guidelines for Finite Element Models and Macros (F4E_D_26W8J4 v1.3).